Materials and Design 188 (2020) 108474

Contents lists available at ScienceDirect

Materials and Design

journal homepage: www.elsevier.com/locate/matdes

Novel design of a coral-like open-cell porous degradable magnesium implant for orthopaedic application

X.Z. Lu, C.P. Lai *, L.C. Chan

Department of Industrial and Systems Engineering, The Hong Kong Polytechnic University, Hung Hom, Kowloon, Hong Kong, China

HIGHLIGHTS

- A novel Mg implant design having a coral-like open-cell porous interior and an outer solid casing was developed successfully
- Implant with 70%~75% porosity and 0.5 mm wall thickness had the optimal structural strength and degradation rate
- Degradation rate of porous interior was significantly faster than that of outer casing due to the nature of porous structure
- The porous structure of the novel implant did benefit the ingrowth of bone tissue and expedite the healing process

GRAPHICAL ABSTRACT

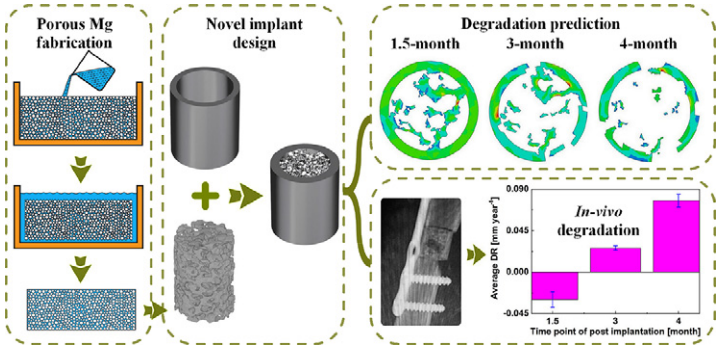

ARTICLE INFO

Article history:
Received 3 July 2019
Received in revised form 18 December 2019
Accepted 4 January 2020
Available online 9 January 2020

Keywords:
Open-cell porous Mg alloys
Continuum damage mechanics
Biodegradation model
Finite element simulation
X-ray computed tomography
In-vivo rabbit model

ABSTRACT

The aim of this study was to use degradation prediction and *in-vivo* evaluation to inspire a novel design of magnesium (Mg) implant having a coral-like open-cell porous interior and an outer solid casing. In this design, the porous interior acts as a bone-mimic channel for tissue infiltration and cell adhesion, while the solid casing enables better structural strength and integrity. Different porosities of porous interiors, combined with different wall thicknesses of outer casing, were designed. By implementing a continuum damage mechanics (CDM)-based biodegradation model into finite element simulations, the mechanical properties and degradation rates of the implant were predicted. The results showed that the implant with 70%–75% porosity and 0.5 mm wall thickness had the optimal structural strength and degradation rate. This implant structure was then fabricated. Compression tests and X-ray computed tomography (CT) scanning were carried out to investigate the material properties and the structural transformation of the implants respectively. Moreover, an *in-vivo* rabbit model was used to evaluate the degradation behaviours of the implant at different time points. The results showed that this novel Mg implant had a relatively sturdy material strength and the porous structure did benefit the ingrowth of bone tissue and expedite the healing process.

1. Introduction

Magnesium (Mg)-based alloys have good potential as biodegradable implant material for *in-vivo* implantation [1–4]. Compared with traditional biodegradable implant materials, such as polymers and bioglass

* Corresponding author.
E-mail addresses: cp.lai@polyu.edu.hk, ise.cplai@connect.polyu.hk (C.P. Lai).

https://doi.org/10.1016/j.matdes.2020.108474

[5,6], Mg-based alloys show their unique characteristics, such as light weight, similar density with bone, and they provide an essential element of the biological system during degradation [7,8]. Also, it is not required to carry out a secondary surgery for implant removal after implantation. It would greatly reduce the patients' risk of health and psychological issues [9]. Several clinical studies of biodegradable Mg alloys have been carried out to evaluate and compare the performance with traditional non-degradable implant materials, such as stainless steel and Ti alloys. The results demonstrated that biodegradable Mg alloys have a good biocompatibility, biodegradability and acceptable mechanical properties. Some specific compositions of Mg alloys were selected and commercially available as bone substitutes/fixation devices [10–13]. Compared with other market-available metallic biomaterials, the elastic modulus and yield strength of Mg-based alloys are closer to those of natural bone. Thus, they can minimize the possible stress shielding and provide adequate mechanical properties [14]. However, the major drawbacks of these Mg implants are their low corrosion resistance and the occurrence of subcutaneous gas cavities after implantation [15]. Alloying with different elements [16,17] and surface modifications [18,19] seems a proper solution to control the degradation rate of Mg alloys for orthopaedic applications. Recent studies reveal that the corrosion resistance of Mg-based alloys could be improved with the formation of a protective zinc phosphate layer during corrosion [20,21]. Moreover, Zn can improve ductility and has little effect on tensile properties. Thus, it can be used to strategically control the corrosion reaction between Mg and body fluid [22]. Rare earth elements have been proposed for alloying to improve the overall degradation rate of Mg-based alloys [23–25]. Previous studies have been performed on these alloys with varying Zn content [26]. It was found that the tensile strength and corrosion resistance of Mg alloy would be improved with increasing Zn content. On the other hand, Mn is an essential element for metabolism of living cells and organism, but over 1% would be shown poisonous effect to cell viability and its proliferation [15,23,27]. Therefore, Mg-3%Zn-1%Mn is the optimal one and thus selected in this study.

To further stimulate the ingrowth of tissue and tailor the density distribution to meet the special requirement of strength, modulus and deformation during implantation, a compelling potential alternative would be the use of porous materials produced by different processes/methods [28,29]. Mg materials with a porous structure have been found to serve as high-potential orthopaedic biomaterials and gained considerable attention for their improved properties from solid structures [30]. These structures are super lightweight, and their elastic moduli are closer to that of natural bones, which would minimize stress shielding and implant loosening. The interconnected pores allow bone tissues, blood vessels and cells to access the voids and provide a large surface area for them to grow, as well as deliver biological factors such as proteins and genes, hence enhancing the formation of new bones. It has been reported that bone ingrowth was faster and deeper for porous implants compared to solid ones [31]. However, the large surface area of a porous structure would also lead to increased Mg oxidation and hence a high degradation rate. In addition, porous structures have weaker tensile strength compared to solid materials; they could easily deform when an external load is applied. Therefore, porous implants with a suitable solid casing would provide better structural integrity and meanwhile control the degradation rate of internal porous implants, thus matching the bone growth rate for better bone recovery.

Normally, the biodegradation of the existing implants is obtained experimentally from *in-vitro* and/or *in-vivo* tests. Such tests are very crucial but rather costly and time-consuming. Also, it is very difficult to achieve biodegradation in *in-vivo* tests because of the complex experimental setups to mimic the human body environment [32]. Eventually, this leads to lengthy and labour-intensive studies, resulting in very low cost/performance ratios. To overcome these long-lasting pre-clinical drawbacks, the finite element (FE) approach is believed to be the most effective in predicting the degradation behaviours of solid-type biomaterials in the living body. At present, there are two main constitutive models, *i.e.*, the physical model formulated with the adoption of Nernst-Planck equation and the continuum damage mechanics (CDM)-based degradation model [33,34]. Deshpande [35] studied the corrosion of some commercially available Mg-based alloys (*e.g.*, AZ91, AZ31, *etc.*) by combining a physical model with adaptive meshing to two-dimensional (2-D) simple geometries. However, only the corrosion of those medical grade alloys with relatively high percentage of Mg (*i.e.*, ≥90%) is considered in this biological study [36]. Wu et al. [37] evaluated and validated the degradation behaviour of absorbable metallic stents (AMS) during a pre-clinical study based on CDM. Grogan et al. [38] proposed an FE corrosion model based on CDM that enables the analysis of corrosion-induced geometric discontinuities on the overall mechanical integrity of specimen. Similarly, Gastaldi et al. [39] developed a continuum damage parameter approach to assess the overall stent damage in terms of heterogeneous corrosion behaviour on an AMS scaffold. By using an adaptive meshing scheme, Grogan et al. [40] developed a more efficient computational FE strategy based on the Arbitrary Lagrangian Eulerian (ALE) adaptive meshing, which can explicitly track the three-dimensional geometry variation of AMS during its corrosion. Although the physical corrosion model has the advantage of describing multi-physics corrosion processes, it lacks the consideration of mechanical property changes against the material's corrosion response [41]. Therefore, it is not so suitable to simulate the biodegradation of a metal implant with complex load-bearing conditions in body implantation. While the CDM-based biodegradation model, which accounts for the reduction in material integrity due to degradation environment and mechanical loading, should be a more appropriate alternative.

Therefore, the main objective of this study was to design a novel biodegradable implant which has the advantages of both solid Mg-3%Zn-1%Mn alloy and its porous structure. In which, the solid casing enables better structural integrity while the porous interior acts as a bone-mimic channel for tissue infiltration and vascularization, benefitting cell adhesion and growth. Different porosities of the porous interior combined with different wall thicknesses of the outer casings of implants were designed; then, FE simulations with the implementation of a CDM-based biodegradation model were performed to predict the mechanical properties and degradation rate of such novel implant structure. Thus, the optimal implant structure was obtained and then fabricated accordingly. Furthermore, compression tests and X-ray CT scanning were carried out to investigate the material properties and the structural transformation of the implants, respectively. Moreover, an *in-vivo* model was performed on the mid-position of a rabbit's humerus to evaluate the degradation behaviours of the implant at different time points. Eventually, it is believed that the open-cell porous Mg implant proposed in this study can provide an effective solution for future design in orthopaedic implantation, which benefits both structural integrity and bone healing.

2. Experimental methods

2.1. Design and preparation of the coral-like open-cell porous Mg implant

In this study, Mg-3%Zn-1%Mn was selected as raw materials of the implant specimens. This composition has been tested by various *in-vitro* studies to verify mechanical and degradation properties, which enables subsequent *in-vivo* tests [27]. The coral-like open-cell porous structure was produced by a modified infiltration method [31] with a water-soluble salt as space holder. In order to meet the functional and strength requirements of the porous structure, the pore sizes and porosity are typically ranged from 0.8 mm to 1.0 mm and 65% to 75% respectively [42–44]. The mixture gases of carbon dioxide and sulphur hexafluoride was applied to prevent oxidation during fabrication. The protective gas was applied to avoid oxidation during the process and to provide an external pressure to drive the molten metal towards the custom-made space holders. The specimens were laundered thoroughly

through a dilute alkaline solution NaOH (0.1 M) [27] after cooling and then sterilized by autoclave for the upcoming experiments.

In this study, the mid-position of a rabbit's humerus was selected to evaluate the degradation of the implanted specimen. As the bone in this region is generally cylindrical, the current study just focuses on a regular tubular structure. Nevertheless, other complex structures will be further studied in the future so as to understand the correlation between the structure and the degradation behaviour. Therefore, the specimens were wire-cut into a cylindrical shape and then assembled to a solid Mg casing with an outer diameter of 5.5 mm and a height of 6 mm. Such size makes the specimen suitable for implantation in the humerus of the selected rabbit model in this study [45]. To ensure the bonding strength between the porous interior and outer solid casing for implantation, interference fit was adopted during the assembly, *i.e.*, the tubular outer casing was heated first to increase its inner diameter, and then the porous interior was inserted into the casing under the external force. Subsequently, the casing was cooled and then bonded tightly with the porous interior. The shear test results show that the bonding strength between porous interior and outer solid casing reached 3.77 MPa, which makes the fabricated implant capable to maintain mechanical integrity during the healing procedure [46–48].

To obtain the optimal structure of the novel implant, different porosities of the porous interior combined with different wall thicknesses of the outer casing of the implant were designed and modelled. The configuration of the implant design refers to Fig. 1, and the detailed structure parameters are shown in Table 1. Then, FE simulations were performed to predict the mechanical properties and degradation rates of these implant structures, and only the optimal implant structure was fabricated for the subsequent *in-vivo* test, thus to reduce the number of trials and adhere to the 3R principles of animal experimentation.

2.2. Hydrogen evolution tests

In order to measure the hydrogen evolution of Mg implants, the modified immersion tests in the simulated body fluid following ASTM G31 [49] were employed and conducted for this hydrogen evolution for Mg-1-3%Zn-1%Mn. The size of the specimens for this test was the same as stated in Section 2.1, *i.e.*, Ø 5.5 mm × 6 mm. Each specimen was immersed in the simulated body fluid with a CO_2-bicarbonate buffer [50] or its equivalent at around 37 °C for approximately 210 h. The changes of hydrogen evolution in the solution were monitored regularly to study the corrosion mechanisms of these specimens. For details of the setup for the measurement of the hydrogen release rate, please refer to our published paper [27].

Table 1
Detailed structure parameters of the novel porous Mg implant.

Numbering	Porosity of porous interior (P)	Wall thicknesses of outer casing (T)
1	65%	0.3 mm
2	70%	0.3 mm
3	75%	0.3 mm
4	65%	0.5 mm
5	70%	0.5 mm
6	75%	0.5 mm
7	65%	0.7 mm
8	70%	0.7 mm
9	75%	0.7 mm

2.3. Compression test and X-ray CT scanning for implant assessment

In this study, the mechanical strength and porous structure of the implant specimen with size of Ø 5.5 mm × 6 mm were evaluated by compression tests and X-ray CT scanning respectively. The compression tests were carried out on an MTS 810 testing machine according to the standard ASTM E9-09 [51]. Compressive loading was applied on the specimen and increased with a controlled speed of 0.1 mm/min until the fracture of the specimen. The stress-strain curves of the material were recorded and plotted; thus, the elastic modulus, yield stress and ultimate compressive stress were obtained to evaluate the strength of the material. In addition, a micro-focus high-resolution X-ray CT system, YXLON FF35 CT, was employed to detect the internal porous structure of the specimen both before and after compression as well as the three-dimensional (3-D) voxel models of those implants at different time points post-implantation. During the X-ray CT scanning, the tube source was operated at 110 kV voltage and 100 μA current; 1800 projections of 2-D X-ray imaging were captured in a 360° rotation, and then 3-D volume CT data were reconstructed using the in-house CERA reconstruction spooler. A high-resolution of 8.9 μm was achieved and such resolution is sufficient enough to detect the degradation process of the internal porous structure of the Mg implant [52]. The profile and porous structure of the specimen were visualized with the aid of VGStudio MAX; thus, the pore size, porosity and degradation rate of the implant specimen were obtained. The compression test and X-ray CT scanning setups are illustrated in Figs. 2 and 3, respectively.

2.4. In-vivo rabbit model for degradation evaluation

In-vivo tests were modified based on standard practice ASTM F763-04 [53]. A total of 12 New Zealand White (NZW) rabbits weighting approximately 2–3 kg and around 2.5 months old were selected as animal models and underwent tests at three time points (*i.e.* 1.5-month, 3-month and 4-month). These animals were divided into three groups,

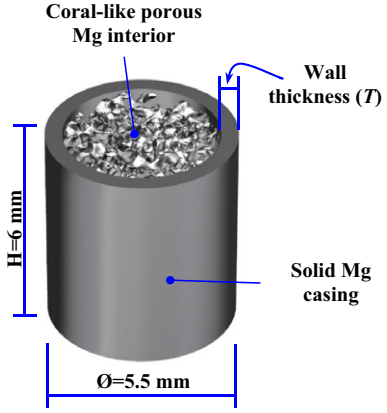

Fig. 1. Configuration of the novel implant design for orthopaedic application.

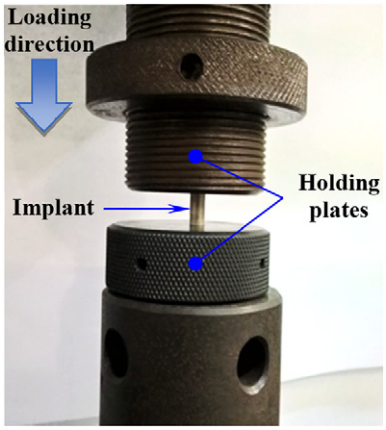

Fig. 2. Setup of the compression test for the implant strength assessment.

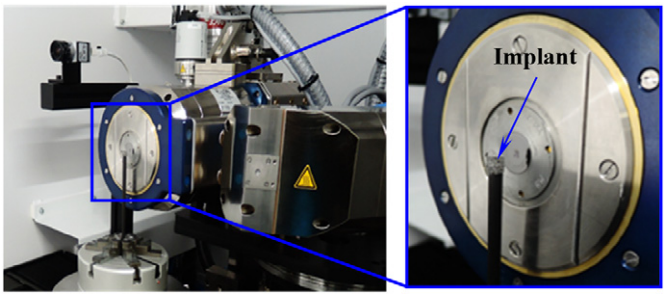

Fig. 3. X-ray CT scanning for the implant using YXLON FF35 CT system.

each group having four animals at each time point, *i.e.*, three animals were implanted, and one animal was served as control. Doses of pre-emptive meloxicam (0.6 mg/kg s/c) and enrofloxacin (5 mg/kg s/c) were injected to the animals prior to surgery. The rabbits were sedated by acepromazine (1 mg/kg, intramuscular injection), followed by intramuscular injection, a mixed solution of ketamine (35 mg/kg) and xylazine (5 mg/kg) was used for anaesthesia and buprenorphine (10 mg/kg) was administered for antibiotic purposes.

An incision/opening with a segmental defect region of 6–8 mm long was created approximately at the midshaft of the LHS humerus of the animal after anaesthesia. The Mg-based porous implant with size of Ø 5.5 mm × 6 mm was then placed at the fracture region and fixed by the usual fixation devices, *i.e.*, one Ti-plate and four Ti-screws. After implantation, the muscles and skin wound were closed by simple suture (absorbable, 4/0, and nylon, 4/0, respectively). During the surgical operation for the Mg implant, as shown in Fig. 4, the inhalation anaesthesia was maintained, followed by an endotracheal intubation with a mixture of isoflurane (2% in volume) and oxygen (0.5 l per min) under spontaneous respiration. The surgical region was stabilized by bandage and checked by X-ray imaging to confirm that the implant is positioned properly after surgery, as shown in Fig. 5, and weekly throughout the implantation. All images were taken under 40 kV for 10-second exposures.

Post-operative care with antibiotics (Enrofloxacin, 10 mg/kg, Subcutaneous injection for five consecutive days) and analgesics (Buprenorphine, 0.01 mg/kg, Subcutaneous injection every 8–12 h for 3–5 consecutive days) was applied to all animals to keep them alive with limited ambulatory procedures. Regular food and water were provided during post-operative care. Special attention was paid for any rabbit that did not consume any water after the surgery. At least 100 ml/day of fluid was injected subcutaneously, and an Elizabethan collar was worn by any animals that have chewed on the incision. At the end of the experimental time point, the rabbits were euthanized and their humerus was harvested for micro-CT analysis. The *in-vivo*

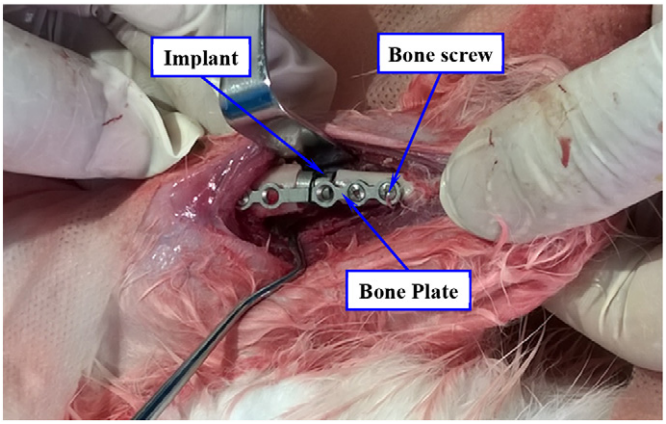

Fig. 4. Photo of the surgical operation for the novel Mg implant implantation.

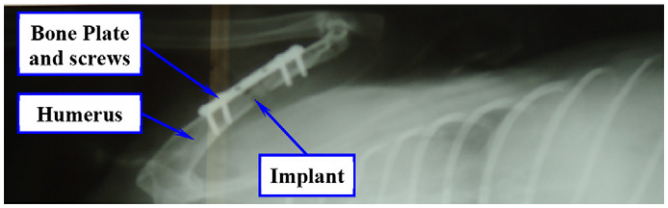

Fig. 5. Radiographic photo of the humerus after surgical operation to check and confirm the implant position (Day 0).

experiments of this study were approved by the Animal Subjects Ethics Sub-committee (ASESC) under approval number 14-15/43-ISE-R-OTHERS and Use of Experimental Animals Permit by The Third Xiangya Hospital of Central South University under approval number of SYXK 2014-0013. Also, it is confirmed that this test was performed in accordance with relevant guidelines and regulations.

2.5. Ex-vivo preparation and X-ray CT scanning for degradation analysis

All animals were anaesthetized by intracardiac injections of acepromazine maleate tranquillizer (1 mg/kg) and sacrificed with an overdose of pentobarbital (Dorminal, 150 mg/kg) *via* intravenous injection at the marginal ear vein at the end of each time point (*i.e.*, 1.5-, 3- and 4-month). The humerus samples with implants and fixation devices were dissociated from the animal by saw. Surrounding soft tissues including skin and muscles were removed and packed in saline wet gauze for performing subsequent *ex-vivo* X-ray CT scanning using the YXLON FF35 CT system with image pixel size ranging from 9 to 18 μm. The reconstructed 2-D and 3-D CT images were acquired and visualized using the software VGStudio MAX. The residual implant was segmented from the surrounding bone using the surface determination function to obtain its volume and surface area. By analysing the constructed CT images of the porous structure, the porosity and pore size of each sample can be measured, while the 3-D shape and geometrical data on the voids/pores and the degraded implant were captured for the subsequent degradation determination.

2.6. Histological procedure

The truncated samples were rinsed by distilled water for 5 min and dehydrated according to the following procedures: dehydrated in 70% isopropyl alcohol for 4 days, in 95% isopropyl alcohol for 4 days with 2 changes and finally in 100% isopropyl alcohol for 4 days with 2 changes. Those dehydrated samples were infiltrated by xylene or its substitutes for pre-embedding process, for 5 days with 2 changes until the tissue sample convert into transparent. After fixation and pre-embedding, the samples were infiltrated with 100% methyl methacrylate (MMA 1) and 100 ml MMA 1 and 2 g dibenzoyl peroxide (MMA 2) for 7 days. Then, the samples were embedded in 100 ml of MMA 2 and 4 g of dibenzoyl peroxide and 25 ml of dibutyl phthalate and placed at a 37degC oven for 7 days for polymerization. The embedded samples were placed at room temperature for hardening. The sample blocks were cut to a section with thickness of 0.3 mm by the diamond cutting band and polished to a thickness of 0.07 mm by a micro-grinding system for staining.

Those bone sections were rinsed in 0.5% acidic alcohol for 30 s to remove the polymerized MMA on the surface. Giemsa solution was freshly prepared by diluting 20 ml of Giemsa (MERCK 1.09204.0100) into 100 ml deionized water and pre-heated at 57degC for 20 min before staining process. The sections were then cleaned by distilled water and dried by filter paper. Giemsa solution was added to the section until the whole embedded surface was covered. The sections with stain were placed at 50 °C for 20 min and washed by distilled water to remove excess stain and acidic alcohol.

To identify the growing bone after *in-vivo* test, Alizarin red staining was employed for calcium staining. Alizarin red dye solution was prepared by dissolving 2 g of Alizarin red S into 100 ml of distilled water and adjusted the pH value between 4.1 and 4.3 by ammonium hydroxide. The bone sections were placed in Alizarin red dye solution for 5 min, rinsed by distilled water to remove excess dyes and dehydrated in 100% propyl alcohol. A very thin glass should be placed over the bone sections to protect and enhance the optical evaluation.

3. CDM-based model for implant biodegradation prediction

Implementing the FE code for biodegradation prediction requires not only the 3-D shape and geometric data about the sponge structure, but also the theoretical biodegradation model. During the implantation for the bone loss region under loading, the Mg-based alloy mostly corroded under the micro-galvanic degradation whereas stress degradation is also very sensitive to the Mg-based alloy because of different load-bearing situations. Concerning a comprehensive model in this study, a modified CDM-based degradation model considering not only micro-galvanic corrosion [41], but also the varying mechanical properties against the degradation response of the porous material, was developed. This CDM-based approach introduces a local damage parameter D, which accounts for a reduction in the mechanical integrity of the material due to degradation. An effective stress tensor $\tilde{\sigma}$ is also introduced. This is expressed as

$$\tilde{\sigma} = \sigma/(1-D) \tag{1}$$

where σ is the undegraded stress tensor. Initially, $D = 0$ indicates that the material is intact while $D = 1$ means the material has been completely degraded and has lost its load-bearing ability. The degradation is assumed to be observable on the free surfaces of the elements, and its evolution is considered on the FE meshes within the geometrical model. The degradation damage parameter D is supposed to be a linear combination of micro-galvanic degradation D_M and stress degradation D_S, formulated as

$$D = D_M + D_S \tag{2}$$

Generally, the evolution law for micro-galvanic degradation can be expressed as

$$D_M = k_M \delta_M / L_e \tag{3}$$

where k_M is the kinetic parameter of the degradation process, which can be obtained through *in-vitro* and *in-vivo* tests by considering biological conditions and degradation responses such as pH, body fluid flow rate, temperature differences, formation of Mg oxides and hydrogen evolution *etc.* δ_M is the material characteristic dimension which contains not only the immersed outer surfaces but also the inner surfaces of the connected pores in the porous structure; L_e is the FE mesh characteristic length. For the axisymmetric element, the L_e can be expressed as

$$L_e = \sqrt[3]{A_e 2\pi l} \tag{4}$$

where A_e is the surface arear of the element and l is the distance from the element centroid to the symmetry axis.

In addition, the evolution law for stress degradation is defined as

$$D_S = (L_e/\delta_S)\left(S\sigma^*_{eq}/(1-D)\right)^R \text{ if } \sigma^*_{eq} \geq \sigma_{th} > 0 \tag{5}$$

$$D_S = 0 \text{ when } \sigma^*_{eq} < \sigma_{th} \tag{6}$$

where σ^*_{eq} represents the equivalent stress and σ_{th} is the threshold value of critical equivalent stress, below which the stress degradation process does not occur. S and R are material constants related to the kinetics of the stress degradation; δ_S is a characteristic dimension of the stress degradation process.

In order to obtain the solution of Eq. (5), an initial state of the moment $t = 0$ is considered, *i.e.*,

$$D_S|_{t=0} = 0 \tag{7}$$

Thus, at a time interval from step n to $n+1$ with a time increment of Δt, the stress degradation can be written as

$$D_S(t+\Delta t) = D_S(t) + (L_e/\delta_S)\left\{1 - \left[1 - \Delta t(R+1)\left(S\sigma^*_{eq}\right)^R\right]^{1/R+1}\right\} \tag{8}$$

The material flow behaviour is described by an elasto-plastic material model. In which, the strain is decomposed as two parts

$$\varepsilon = \varepsilon^e + \varepsilon^p \tag{9}$$

where ε^e and ε^p represent the elastic and plastic parts, respectively.

According to the classical Mises-type theories of metal plasticity, the flow rule of ε^p can be given by [54]

$$\varepsilon^{\mathrm{p}} = \sqrt{\frac{3}{2}} p \mathbf{N} = \sqrt{\frac{3}{2}} \left\langle \frac{F_y}{K} \right\rangle^n \mathbf{N} \tag{10}$$

where $\dot{p}$ is the accumulated plastic strain rate, K and n are the material viscosity parameters. $\langle\rangle$ is the McCauley operator; $\mathbf{N}$ is the unit vector of the yield surface F_y. And the F_y can be written as

$$F_y = \sqrt{\frac{3}{2}} \|\tilde{\sigma}'\| - Q, \tag{11}$$

where Q is the deformation resistance which follows the isotropic hardening rule, and its specific form is

$$Q = Q_0 + Q_s, \tag{12}$$

where Q_0 and Q_s are the initial and the subsequent deformation resistances, respectively.

The evolution law of the resistance Q_s can be expressed as

$$\dot{Q}_s = \beta(Q_s^{\mathrm{sat}} - Q_s)\dot{p}, \tag{13}$$

where Q_s^{sat} is the saturated value of Q_s, β controls the evolution rate of Q_s.

The proposed CDM-based biodegradation model can be implemented within an FE package (*e.g.* ABAQUS) by developing a user-defined material subroutine (VUMAT). A flowchart for the VUMAT is shown in Fig. 6. For the FE simulations, the geometrical model of the

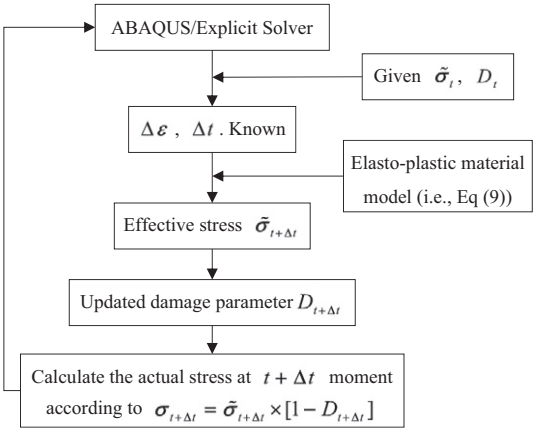

Fig. 6. Flow chart of the CDM-based biodegradation model VUMAT.

implant was meshed with 3D 4-node linear tetrahedral elements (C3D4). Compressive loading was imposed on the top surface of the porous geometrical model to mimic the load-bearing conditions during implantation. It is assumed that only elements on the external or exposed surfaces are degraded. *D* of an element reaches 1 means the element is completely degraded. Then the element will be removed from the mesh set, its neighbouring elements become new degradation surfaces. The ALE implementation can also be achieved using ABAQUS/Standard combining user subroutines UMESHMOTION, UETERNALDB and UFIELD [40]. It has been proved to be more efficient and less mesh-sensitive than those element removal approaches. By moving the facet along its inward-pointing normal, the facet velocity *v* can be determined. The prediction of CDM-based biodegradation can then be presented in terms of the quantity *vt*, which is the degradation rate multiplied by degradation/immersion time. This can be considered an equivalent one-dimensional 'biodegradation distance'. In this study, the 3-D shape and geometric data on the voids/pores inside the porous structure obtained from the X-ray CT system was input into the FE code. The kinetic parameters and characteristic dimensions obtained through *in-vitro* and *in-vivo* tests, as well as the material constants (*i.e.*, relative density, elastic modulus *E*, anisotropic hardening parameters, *etc.*) acquired from compressive tests, were employed in the CDM-based biodegradation model.

4. Results and discussions

4.1. Predicted material properties and degradation rates of different implant structures

The predicted material properties (*i.e.*, elastic modulus, yield strength and ultimate compressive strength) of the porous implants with different porosities of the porous interior and wall thicknesses of the outer casing are shown in Fig. 7. It can be seen that the elastic modulus and strength of the implants decreased with an increase in porosity at a specific wall thickness of the outer casing. In addition, these properties clearly increased as the wall thickness increased at a specific porosity of the porous interior. Therefore, it can be concluded that lower porosity and a thicker outer casing allow for better strength and higher modulus of the implant. To meet the requirements of the implant's yield strength and the ultimate compressive strength (black dash and dash dot lines shown in the figure), the predicted strength values should be above the black dash lines, thus implants 4–9 are the desired specimens. In addition, to ensure that the implant modulus is close to the natural bone, *i.e.*, the predicted modulus values are preferably near the blue dash line, implants 4–6 are further selected. Therefore, porous implants with 0.5 mm thickness of the outer casing and 65%–75% porosity of the porous interior are the most suitable structure for the material property requirement.

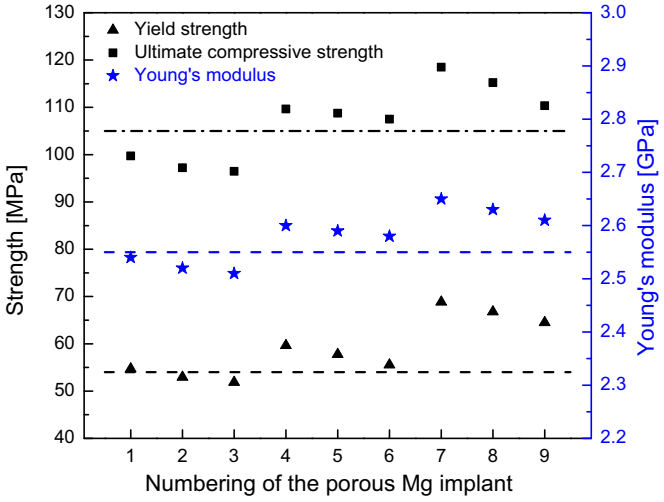

Fig. 7. Predicted material properties of the porous Mg implants with different structures. The blue dash line indicates the required Young's modulus of the implant; The black dash and dash dot lines represent the required yield strength and ultimate compressive strength of the implant, respectively.

Before the implementation of the FE model for degradation prediction, the CDM-based degradation model was calibrated based on the results of *in-vitro* tests. Details of the setup of *in-vitro* test can be referred to our published work [23–27]. Structure of implant 4 was selected and the material parameters involved in the degradation model are listed in Table 2. The stress-strain relation and mass loss from the FE degradation model at different time-points were compared with the observed *in-vitro* tests in Figs. 8 and 9 respectively. It can be seen that the CDM-based degradation model is capable of capturing the experimental mechanical response and mass loss rate of the implant over time.

Furthermore, implants 4, 5 and 6 were used for degradation prediction (see Fig. 10). To better reveal the internal structure of these implants, one typical 2-D section from each implant was extracted, and the predicted degradation results of these sections at different time points are shown in Fig. 11. It was found that the outer casings of these implants were basically not degraded until the 1.5-month time point, and then they were degraded slowly, but most of them remained until the 4-month time point. For the porous interiors with different porosities, they degraded faster than the outer casing, and most of them had degraded by the fourth month. More specifically, implant 4, with a porosity of 65%, had the most undegraded porous interior during the 4-month implantation, while the outer solid casing degraded the most. The reason may be that the fewer internal channels of implant 4 causes the degradation to be shifted from the porous interior to outer solid casing, thus accelerating the degradation of outer solid casing. However, when the porosity of the implant increases to 70% or more (*i.e.*, implants 5 and 6), the porous interior almost completely degraded, but the outer solid casing had the most remaining. Since the rapid degradation of the porous interior would be conducive to the growth of bones and tissues, and the remaining outer solid casing would ensure the strength and the stability of the implant during the whole implantation period, implants 4 and 5 can be considered to have the most suitable structure for orthopaedic application. Hence, implants with *P* of 70%–75% and *T* of 0.5 mm were fabricated accordingly for the subsequent mechanical test and *in-vivo* assessment.

4.2. Implant strength, structural and hydrogen evolution assessment

The stress-strain curve of the porous Mg implant, as well as the physical pictures of the implant sample at three typical strain levels (*i.e.*, 0, 0.085 and 0.112), are shown in Fig. 12. In addition, the stress-strain curve of the complete porous Mg specimen is also shown in Fig. 12 for comparison. It can be seen that the yield strength of the implant increases significantly from 5.9 MPa to 58.3 MPa when the outer solid casing is adopted, and such increase in strength is just slightly lower than that of complete solid casting structure [15]. This would conducive to the stability of the implant during implantation. During the test, the Mg implant could be steadily compressed to 0.085 strain with a maximum stress of 110 MPa. There was then a sudden decrease in stress accompanied by cracking of the casing at the top of the implant, indicating a brittle fracture of the outer solid casing. After that, the casing was no longer protective, and the porous Mg interior would endure compressive loading until 0.112 strain.

The microstructure of the fabricated specimen is shown in Fig. 13. The outer tubular casing was made by extrusion process; thus, a refined structure could be observed with the average grain size of 15–30 μm. On the other hand, the average grain size of inner porous Mg was 100–200 μm. This phenomenon could be explained by the ingot after

Table 2
Material parameters for the degradation model prediction.

k_M	δ_M	σ_{th}	S	R	δ_S	Q_0	Q_s^{sat}	β	K	n
0.005	0.1 mm	95 MPa	0.007 mm^{-2} $h^{-0.5}$ N^{-1}	2	0.07 mm	55.4 MPa	52.5 MPa	2.5	30	6.2

melt and cooled under the faster cooling rate, the surface of the ingot during semi continuous casting impedes the primary crystal grain growth caused the coarse grain structure. Furthermore, Fig. 14(a) shows the 2-D CT images of the un-deformed implant specimen. It was observed that the shape of the internal pores was close to spherical, and the average pore size and porosity were 1.02 mm and 68.2%, respectively. Furthermore, the 2-D CT images of the deformed specimen at strains of 0.085 and 0.112, were constructed. It was found that the average pore size of the porous structure remained almost unchanged during deformation, indicating that stress was mainly applied to the casing instead of the porous structure. After 0.085 strain, the casing cracked, and hence, the porous structure began to be compressed, and the pore size and porosity decreasing slightly to 1.01 mm and 10%, respectively.

These results indicate that the strength of the implant structure was sufficient for implantation applications. In addition, the calculated elastic modulus from repeated compression tests of the specimen is 2.58 GPa, which is closer to that of natural bone and can thus minimize stress shielding. The ultimate compressive strength of the implant is 110 MPa, which is similar with the strength of animal bones (107 ± 1.6 MPa) [55]. Referring to the 2-D CT images, the casing and pore could withstand a strain of 8.5% with very small deformation; after that, the protection of the casing becomes invalid, and the porous structure endures the external load. During the recovery period, the implant together with fixation devices were provided sufficient mechanical support to fix the fractured bones. The mechanical robustness is a critical factor in the design of orthopaedic applications.

In addition, the hydrogen evolution of Mg-1-3%Zn-1%Mn is illustrated in Fig. 15. In general, the hydrogen gas was released steadily over the immersion period, but the steeper slope was found in the middle stage of the test (time = 50–100 h) for specimen Mg-2%Zn-1%Mn. It was observed that the solid case was corroded first at the initial stage (time = 0–50 h) and the porous structure was then corroded to accelerate the overall hydrogen release rate. As the immersion time increased, the corrosion rates of specimens Mg-1%Zn-1%Mn and Mg-3%Zn-1%Mn were slowed down because the protective zinc phosphate layers were formed at the later stage of the test (time > 100 h) [56,57]. The reactions between magnesium, zinc and phosphate in the simulated body fluid are shown as below:

$$3Mg + 2H + 2H_2PO_{4-} \rightarrow Mg_3(PO4)_2 + 3H_2 \quad (14)$$

$$3Zn^{2+} + 2H_2PO^{4-} + 2H^+ + 4H_2O + 6e^- \rightarrow Zn_3(PO_4)_2 \cdot 4H_2O + 3H_2 \quad (15)$$

However, the overall hydrogen release rate of specimen Mg-2%Zn-1Mn was increased during the same period. This phenomenon can be explained by the competition between formation of the protective film and degradation of the Mg alloy; the degradation was dominant in the process. In short, only Mg-3%Zn-1%Mn exhibited a stable and relatively low hydrogen evolution rate. Based on the above findings, the proposed implant design with Mg-3%Zn-1%Mn was able to fulfil the mechanical robustness and hydrogen evolution requirements and the subsequent *in-vivo* analysis was then carried out.

4.3. In-vivo assessment

As stated in Section 2.4, a total of 12 rabbits were used for the *in-vivo* assessment. One of them died from loss of appetite, and plate dislocation was observed 2 weeks after surgery. Due to severe plate bending and pin dislocation caused by overweight, malunion of bone was found in another rabbit. The rest of the 10 animals exhibited normal mental health and wound recovery during the observation period. The mobility of all animals recovered seven days after the surgery, and their weight steadily increased. The weight change of all rabbits during the *in-vivo* test is shown in Table 3.

4.4. X-ray radiography

Fig. 16 shows the X-ray radiographs of the tested animals after surgery (Day 0, 1.5-month, 3-month and 4-month post-operation). It was found that almost no gas bubbles were observed after implantation due to the special characteristics of the implant structure, *i.e.*, the porous structure was first degraded, and hydrogen gas was generated in the porous channels and was trapped by the solid casing. The hydrogen gas

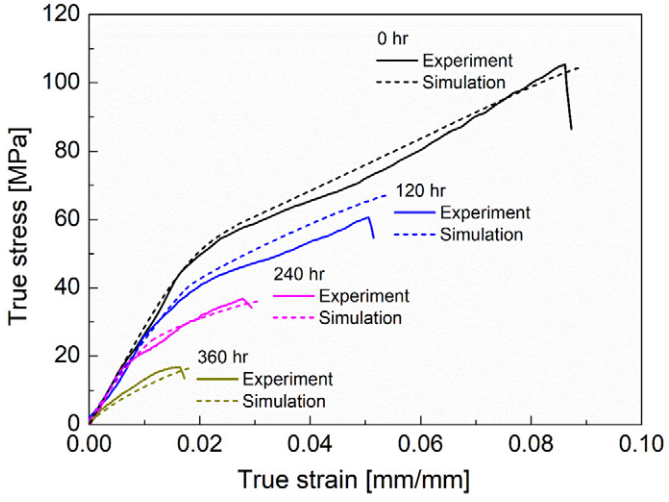

Fig. 8. Stress-strain curves for the original and degraded porous Mg implants based on *in-vitro* tests and FE simulations at different time-points.

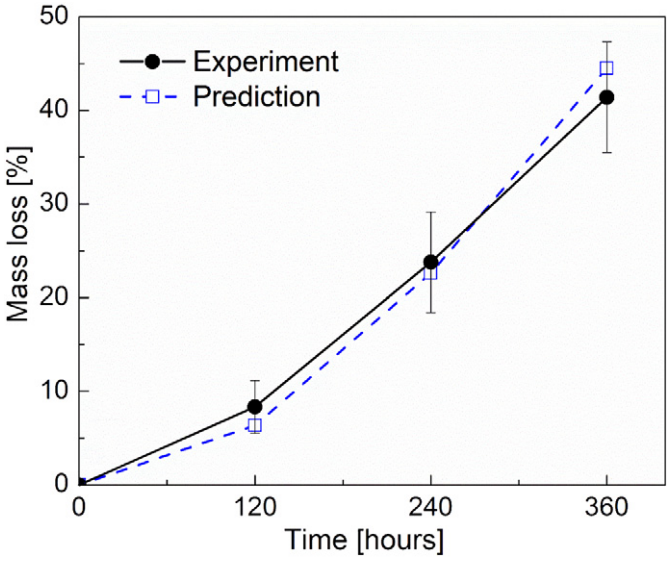

Fig. 9. Percentage of mass loss over time obtained from FE predictions and *in-vitro* tests.

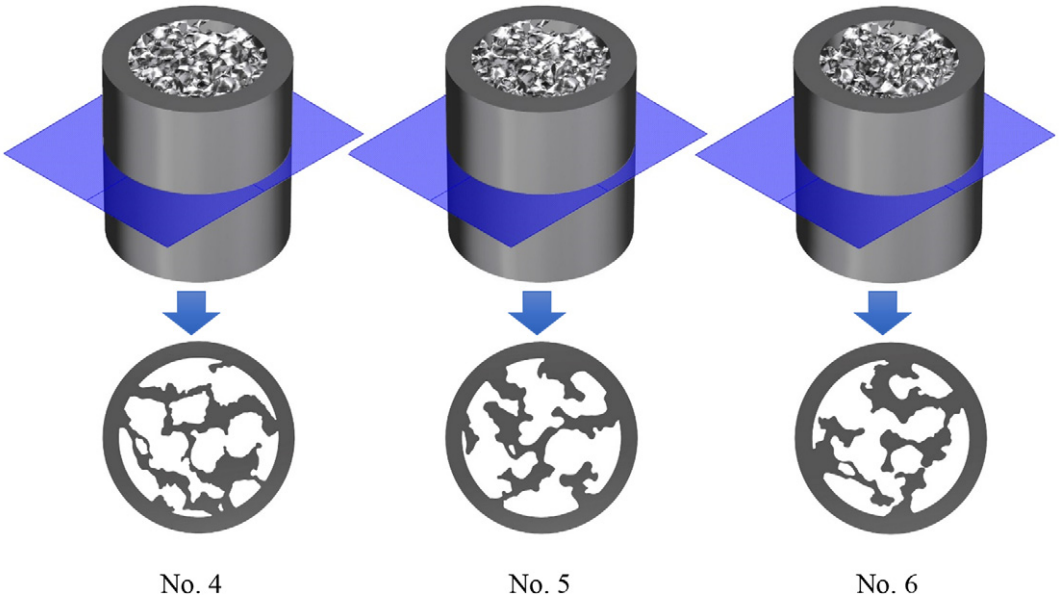

Fig. 10. Typical 2-D sections of the selective implants (nos. 4, 5 and 6) for the degradation process analysis of their internal structures.

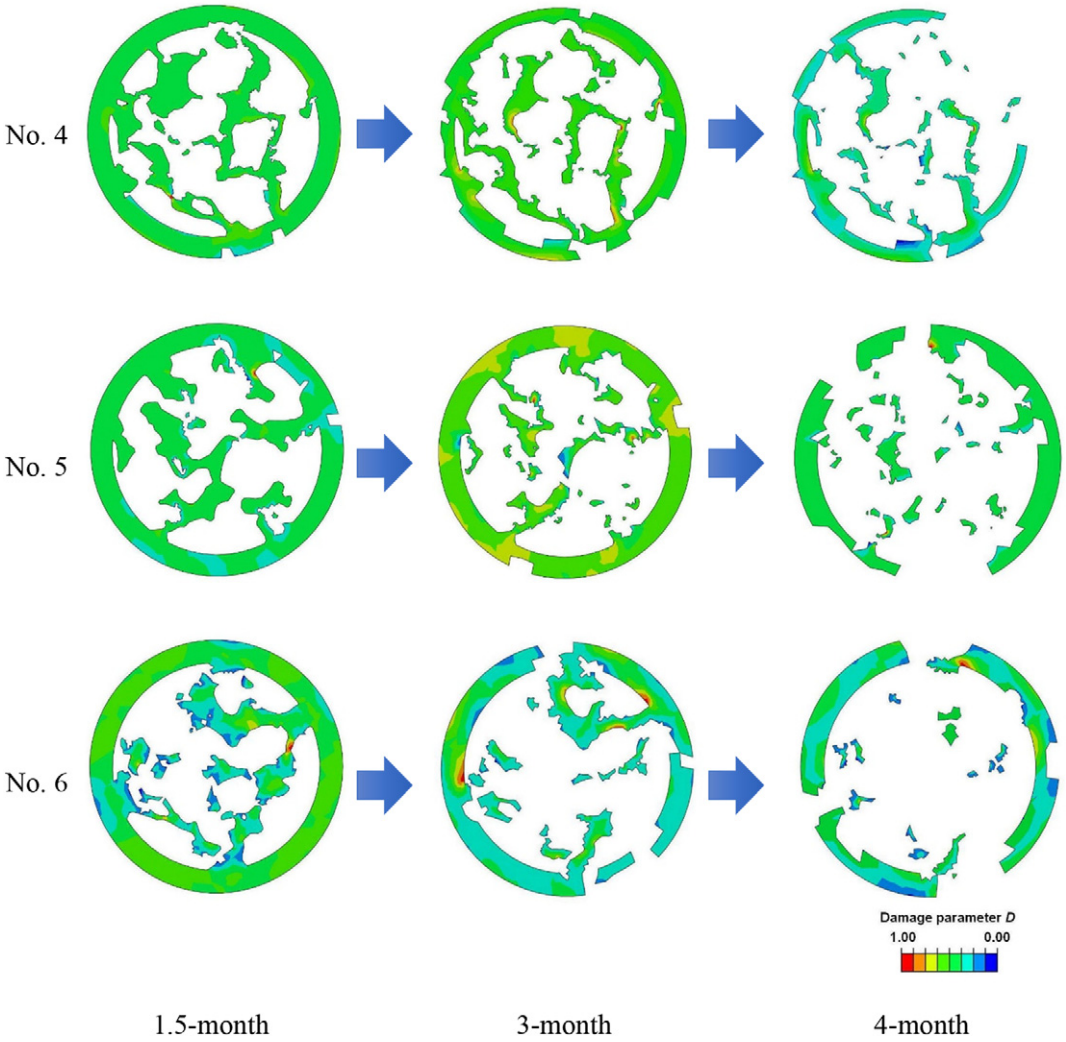

Fig. 11. The simulated degradation processes of the 2-D sections for implants 4, 5 and 6 at 1.5-, 3- and 4-month time points. The damage parameter *D* indicates how much the element degraded (0 = no damage; 1.0 = totally damaged).

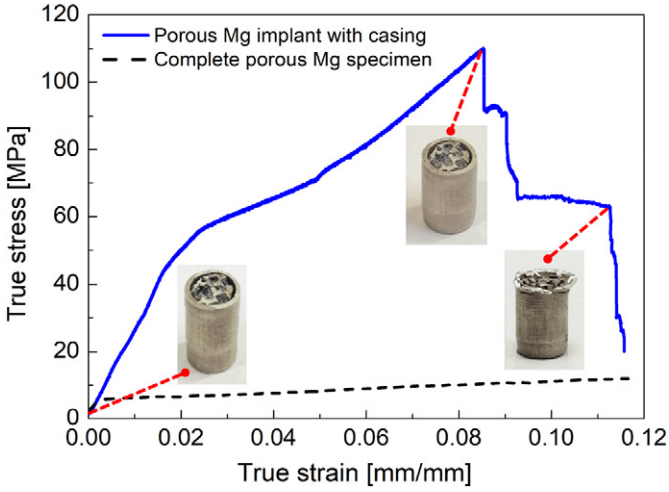

Fig. 12. Stress-strain curves of the porous Mg implant and the complete porous Mg specimen, as well as the physical pictures of the implant sample at three typical strain levels (*i.e.*, 0, 0.085 and 0.112).

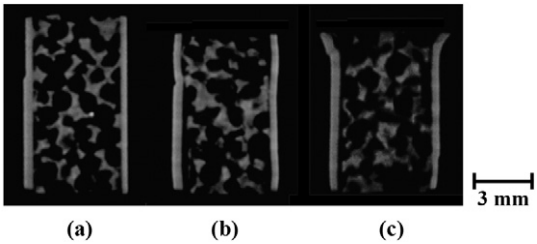

Fig. 14. 2-D X-ray CT images of the porous Mg implant at compressive strains of (a) 0, (b) 0.085 and (c) 0.112.

was then dissolved in the blood/body fluid nearby and absorbed by the body through the blood circulation. Compared to porous interior, the degradation rate of the solid casing was relatively slow due to oxidation films were formed during the degradation process and improved the corrosion resistance of implant [58,59]. The implant degraded steadily, and bone tissue growth was observed at the defect region. Bone continuity was observed in the 3-month and 4-month groups but not in the 1.5-month group. Compared with other findings [60,61], gas film formation depends on the chemical composition and the dimension of specimens. Also, soft callus formation was observed at 1.5-month; the implant was surrounded by a small amount of soft tissues, however, very less of soft tissues can be found around the bone defect region in the control group. The overall size of the defect region was becoming larger, which is double the original bone diameter. This could be explained by the occurrence of intramembranous ossification and bone tissue being formed from the edge of the defect gap towards the centre. A bone cuff was formed around the defect region; the implant was totally enclosed by fibrous tissue and cartilage. The bony bridge was initially formed by soft callus, and the overall size of such bone cuff was 2.5 times the original bone diameter at 3-month group. In the control group, soft callus was formed at the defect region, but the overall size of bone cuff was 1.5–2 times at the same time point. Bone integrity was not observed at this stage. Hard callus formation was observed in the 4-month group and bone continuity improved. No gap was observed at the defect region. The overall dimension of the defect region was reduced and stable, and bone remodelling was beginning. The similar phenomenon was observed in the control group. However, bone continuity could not be improved until 4-month post-implantation.

4.5. Degradation and histological analysis of the implant

To obtain the experimental degradation rate, the harvested humerus samples together with the surrounding tissues and residual implants at 1.5, 3- and 4-month post-implantation were scanned by a high-resolution X-ray CT system. 3-D voxel models of the whole implant under *in-vivo* test at different time points could be visualized after reconstruction, as shown in Fig. 17. Since degradation mainly occurred at the porous interior of the implant, the porous structures inside the outer casing were also extracted and shown in Fig. 17. A slight degradation was observed at the porous interior after 1.5-month post-implantation. The overall volume and structure of the porous interior were still identified. At 3-month post-implantation, degradation still occurred, and all sharp regions of the casing were corroded. On the other hand, the porous structure corroded significantly, and it was hard to distinguish the pore distribution. At 4-month post-implantation, the porous structure could no longer be identified, and most of it had degraded.

The residual volume of each implant sample was measured and obtained after 3-D reconstruction which was segmented from the surrounding bone using the surface determination function to obtain its

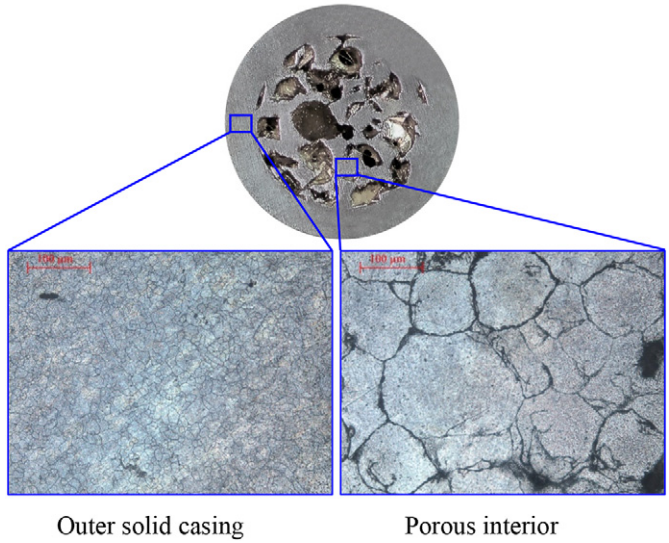

Fig. 13. The microstructure of the fabricated porous Mg implant.

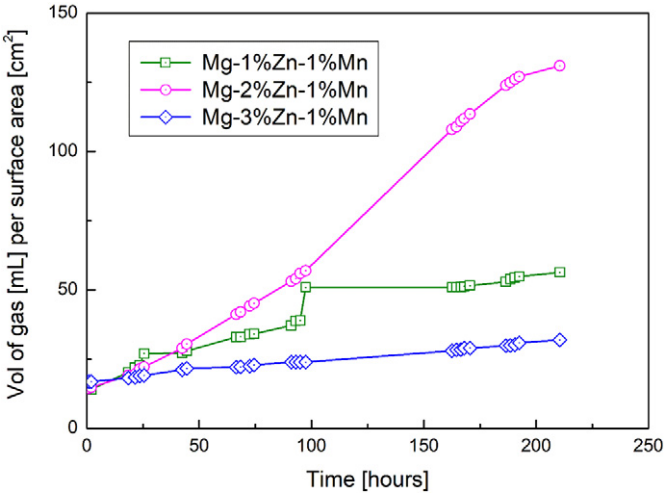

Fig. 15. Hydrogen evolution of Mg-1-3%Zn-1%Mn specimens.

Table 3
Weight comparison of all tested animals during the *in-vivo* test.

Time point	Label	Weight (kg)		Difference (%)	Remark
		Initial	Final		
1.5-month	2D	3.10	3.58	+15.48	
	2E	3.34	3.55	+6.28	Severe plate bending and pin dislocation
	2F	3.04	3.38	+11.18	
	2G	2.30	2.58	+12.17	Control
3-month	3D	2.22	3.36	+51.35	
	3E	2.38	3.54	+48.74	
	3F	2.02	2.21	+9.40	Died during the test
	3G	1.94	3.16	+62.89	Control
4-month	1D	2.28	3.49	+53.07	
	1E	2.28	3.54	+55.26	
	1F	2.42	3.46	+42.98	
	1G	2.18	3.04	+39.44	Control

volume and surface area. According to ASTM G31-72, the averaged degradation rates were calculated using Eq. (6):

$$DR\ (\text{mm year}^{-1}) = \Delta V/SA \cdot t \tag{16}$$

where DR is the degradation rate, ΔV is the change in volume, SA is the implant surface area and t is the implantation time. The average degradation rates for the Mg implants were calculated in millimetres per year (mm year^{-1}), assuming uniform degradation. Although localized degradation occurs *in-vivo* test, this assumption has been widely used for simplistic measurements.

The calculated degradation rate of the whole implant using Eq. (16) is shown in Fig. 18. It was found that the degradation rates differ at different post-implantation time points. The findings reveal that the volume of the whole implant at 1.5-month post-implantation had slightly increased and led to a negative degradation rate (−0.0296 mm year^{-1}). This could be explained by the formation and degradation of a protective $Mg(OH)_2$ layer which served as a barrier to protect the casing and porous structure. It leads to a relatively slow degradation rate and minimize hydrogen evolution during the 1.5- to 3-month implantation. From the reconstructed 3-D X-ray CT images in Fig. 17, implant surfaces in contact with the body fluid, *i.e.*, the top and bottom of the implant, showed initial signs of degradation. Surfaces in contact with bones were less susceptible to degradation, as the bones provided protection for the implant. The average degradation rate then increased to 0.0263 mm year^{-1} at the 3-month implantation, which could be attributed to the gradual degradation of the internal porous structure. It should be noted that the changes in volume include not only the degradation of the implant itself but also the newly grown bone tissue inside the porous structure, and this makes the overall degradation rate of the implant much slower than that of the *in-vitro* test. At the 4-month implantation, there was a rapid increase in degradation rate (0.0777 mm year^{-1}) because of the breakdown of these $Mg(OH)_2$ layers and the further fast reaction between Mg and tissue fluid, and such cyclic reaction will continue until the implant vanished. Since the reaction of Mg was very active, it kept degrading to release a large amount of Mg ions and Mg chlorides to the surrounding region, which stimulates bone tissue growth at the defect region.

In addition, it was found that the degradation rates of the porous interior were significantly faster than that of the outer casing, and thus the porous interior contributes to most of the degradation of the entire implant. Therefore, the degradation of the porous interior plays a predominant role to controlling the degradation process of the whole implant throughout the implantation period. These results were expected because of the nature of the porous structure [62], whose interconnected pores provided channels to enable the flow of body fluids, thus resulting in accelerated degradation of the implant and meanwhile benefitting the ingrowth of bone tissue and expediting the healing process.

The histological analysis showed that an abundant of calcified callus was spread around the implant with a thin gas film after 3 months post-implantation, see Fig. 19. It was observed that the bone growth around the implant and segmental defect location was promoted and stimulated by magnesium ions. However, the degradation rate of porous structure (interior part) and the solid casing (outer part) was not uniformity. The porous structure was first degraded, and gas was trapped by the solid casing. The hydrogen gas was dissolved in the blood and absorbed by the body through the blood circulation. An opaque by-

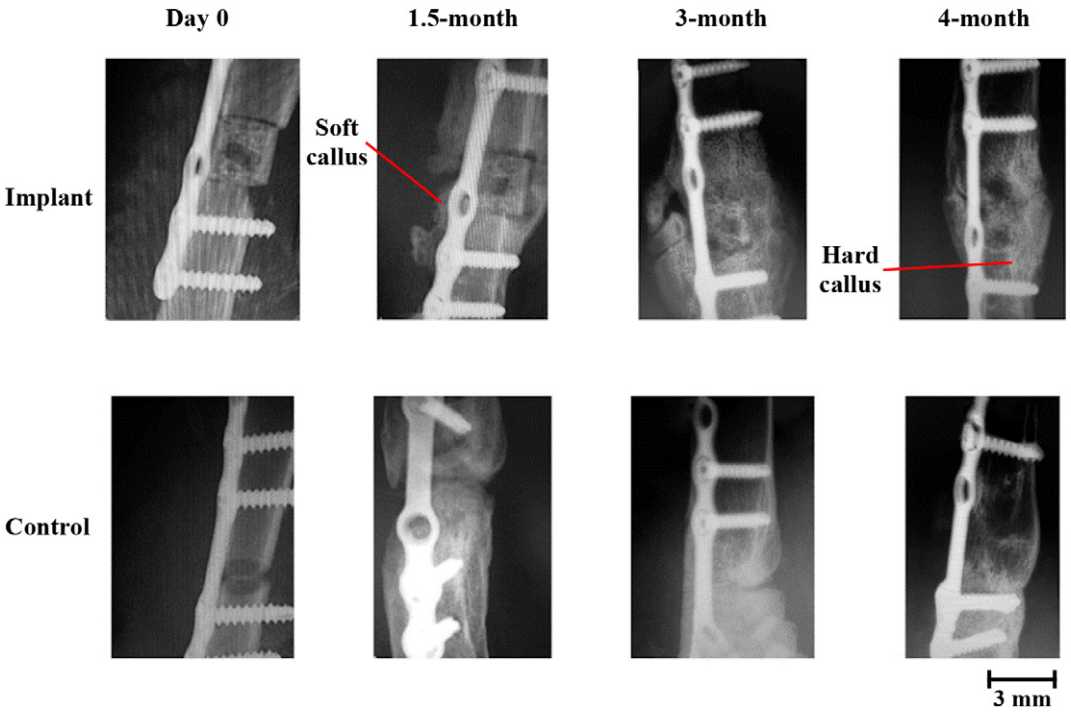

Fig. 16. X-ray radiographs of the porous Mg implant (upper row) and control (lower row) after the surgery (Day 0, 1.5-, 3- and 4-month post-implantation).

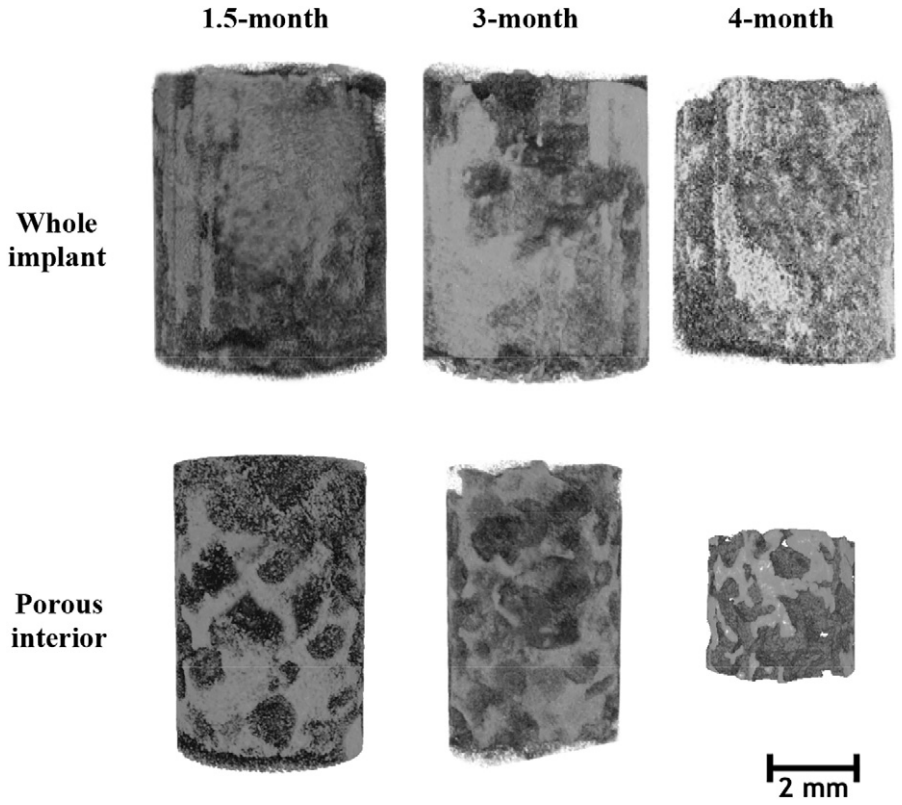

Fig. 17. 3-D voxel models of the whole implant and porous interior under *in-vivo* test at different time points (1.5-, 3- and 4-month).

product was observed at the porous section while the case was fairly complete after 3 months post-implantation. Moreover, the degradation rate of the solid case was relatively slow compared with the porous structure. It is because oxidation films were formed during the degradation process and improved the overall corrosion resistance of the implant [59,60]. A thin layer of gas film between the implant and newly formed calcified callus could be observed near the outer casing after 3 months post-implantation. Such gas film was in favour of the bone tissue adhered on the implant and hinder the bone tissue. The average size of gas film was then reduced and dispersed at 4 months post-implantation which the gas was absorbed by surrounding tissues and enter to the bone remodelling stage.

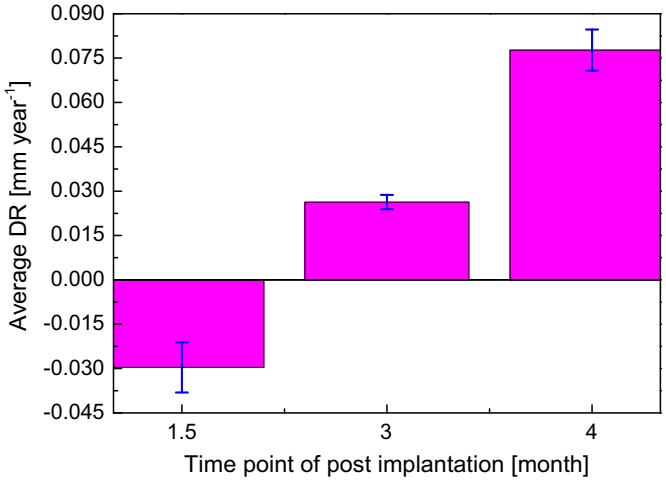

Fig. 18. Degradation rate of the novel Mg implant at 1.5-, 3- and 4-month post-implantation.

5. Conclusions

This study successfully developed a novel Mg implant structure design having a coral-like open-cell porous interior and an outer solid casing. The configuration of the implant was designed and optimized with the aid of FE simulations. The results indicated that the novel implant with 0.5 mm thickness of the outer casing and 70%–75% porosities of the porous interior was the most suitable structure for the material properties and degradation requirements. The optimal structure of the implant was then fabricated with a strength of 110 MPa, which was sufficient for implantation applications, and the measured elastic modulus was 2.58 GPa, which is closer to those of natural bone and thus can minimize stress shielding. In addition, X-ray CT scanning showed that the average pore size and porosity of the implant were 1.02 mm and 68.2% respectively, and the structural transformation analysis demonstrated that the casing could withstand as a protective layer under the strain of 8.5% with very small deformation.

Furthermore, the results of X-ray radiography revealed that the novel Mg implant was degraded steadily. Bone continuity was not observed in the 1.5-month group but it was seen in the 3-month and 4-month groups. At the 4-month implantation, the hard callus formation was observed, the bone continuity had improved, the overall dimension of the defect region had reduced, and the bone remodelling was beginning. The results of X-ray CT scanning showed that the volume of the whole implant at 1.5-month post-implantation had slightly increased and led the negative degradation rate (-0.0296 mm year^{-1}) due to the formation and degradation of protective $Mg(OH)_2$ layers. The average degradation rate then increased to 0.0263 mm year^{-1} at 3-month time point, which could be attributed to the gradual degradation of the porous interior. At 4-month time point, there was a rapid increase in degradation rate (0.0777 mm year^{-1}) due to the breakdown of these $Mg(OH)_2$ layers, and a further fast reaction between the Mg and tissue fluid. In addition, it was found that the degradation rates of the porous interior were significantly faster than those of the outer casing

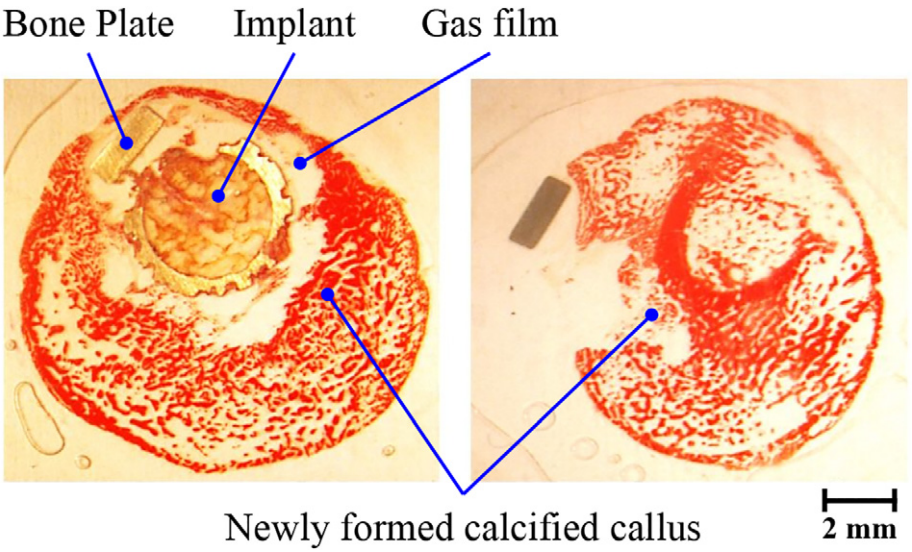

Fig. 19. Histological macro-photographs of Alizarin red S staining of the formed calcified tissue after 3 months post-implantation.

due to the nature of the porous structure, whose interconnected pores provided channels to enable the flow of body fluids. This resulted in accelerated degradation of the implant, meanwhile benefitting the ingrowth of bone tissue and expediting the healing process.

CRediT authorship contribution statement

X.Z. Lu: Methodology, Formal analysis, Investigation, Data curation, Writing - original draft, Writing - review & editing. **C.P. Lai:** Formal analysis, Investigation, Data curation, Writing - review & editing, Validation. **L.C. Chan:** Conceptualization, Supervision, Resources, Project administration, Funding acquisition.

Declaration of competing interest

The author(s) declare no competing interests.

Acknowledgements

The work described in this paper was partially supported by a grant from the Research Committee of The Hong Kong Polytechnic University under account code G-YBRL and a grant from the Research Grants Council of the Hong Kong Special Administrative Region, China (Project No. PolyU 511511). Partial result of this article had been presented in the International Conference on the Technology of Plasticity (ICTP 2017).

References

[1] F. Witte, V. Kaese, H. Haferkamp, E. Switzer, A. Meyer-Lindenberg, C.J. Wirth, H. Windhagen, In vivo corrosion of four magnesium alloys and the associated bone response, Biomaterials 26 (2005) 3557–3563.
[2] B. Heublein, R. Rohde, V. Kaese, M. Niemeyer, W. Hartung, A. Haverich, Biocorrosion of magnesium alloys: a new principle in cardiovascular implant technology? Heart 89 (2003) 651–656.
[3] Z. Tang, H. Huang, J. Niu, L. Zhang, H. Zhang, J. Pei, J. Tan, G. Yuan, Design and characterizations of novel biodegradable Zn-Cu-Mg alloys for potential biodegradable implants, Mater. Des. 117 (2017) 84–94.
[4] N. Li, Y. Zheng, Novel magnesium alloys developed for biomedical application: a review, J. Mater. Sci. Technol. 29 (2013) 1–14.
[5] L.N. Novikova, L.N. Novikov, J.O. Kellerth, Biopolymers and biodegradable smart implants for tissue regeneration after spinal cord injury, Curr. Opin. Neurol. 16 (2003) 711–715.
[6] D. Vukajlovic, J. Parker, O. Bretcanu, K. Novakovic, Chitosan based polymer/bioglass composites for tissue engineering applications, Mater. Sci. Eng. C 96 (2018) 955–967.
[7] S.M. Kayhan, A. Tahmasebifar, M. Koç, Y. Usta, A. Tezcaner, Z. Evis, Experimental and numerical investigations for mechanical and microstructural characterization of micro-manufactured AZ91D magnesium alloy disks for biomedical applications, Mater. Des. 93 (2016) 397–408.
[8] H.R. Bakhsjeshi-Rad, M.H. Idris, M.R. Abdul Kadir, S. Farahany, Microstructure analysis and corrosion behavior of biodegradable Mg-Ca implant alloys, Mater. Des. 33 (2012) 88–97.
[9] T. Kraus, S.F. Fischerauer, A.C. Hänzi, P.J. Uggowitzer, J.F. Löffler, A.M. Weinberg, Magnesium alloys for temporary implants in osteosynthesis: in vivo studies of their degradation and interaction with bone, Acta Biomater. 8 (2012) 1230–1238.
[10] J.M. Seitz, A. Lucas, M. Kirschner, Magnesium-based compression screws: a novelty in the clinical use of implants, JOM 68 (2017) 1177–1182.
[11] C. Plaass, C. von Falck, S. Ettinger, L. Sonnow, F. Calderone, A. Weizbauer, J. Reifenrath, L. Claassen, H. Waizy, K. Daniilidis, C. Stukenborg-Colsman, Henning Windhagen, Bioabsorbable magnesium versus standard titanium compression screws for fixation of distal metatarsal osteotomies—3 year results of a randomized clinical trial, J. Orthop. Sci. 23 (2018) 21–327.
[12] R. Biber, J. Pauser, M. Brem, H.J. Bail, Bioabsorbable metal screws in traumatology: a promising innovation, Trauma Case Reports 8 (2017) 11–15.
[13] D. Zhao, F. Witte, F. Lu, J. Wang, J. Li, L. Qin, Current status on clinical applications of magnesium-based orthopaedic implants: a review from clinical translational perspective, Biomaterials 112 (2017) 287–302.
[14] J. Nagels, M. Stokdijk, P.M. Rozing, Stress shielding and bone resorption in shoulder arthroplasty, J. Shoulder Elb. Surg. 12 (2003) 35–39.
[15] E. Zhang, D. Yin, L. Xu, L. Yang, K. Yang, Microstructure, mechanical and corrosion properties and biocompatibility of Mg-Zn-Mn alloys for biomedical application, Mater. Sci. Eng. C 29 (2009) 987–993.
[16] X. Liu, J. Sun, F. Zhou, Y. Yang, R. Chang, K. Qiu, Z. Pu, L. Li, Y. Zheng, Micro-alloying with Mn in Zn–Mg alloy for future biodegradable metals application, Mater. Des. 94 (2016) 95–104.
[17] K. Bobe, E. Willbold, I. Morgenthal, O. Andersen, T. Studnitzky, J. Nellesen, W. Tillmann, C. Vogt, K. Vano, F. Witte, In vitro and in vivo evaluation of biodegradable, open-porous scaffolds made of sintered magnesium W4 short fibres, Acta Biomater. 9 (2013) 8611–8623.
[18] D.B. Prabhu, P. Gopalakrishnan, K.R. Ravi, Coatings on implants: study on similarities and differences between the PCL coatings for Mg based lab coupons and final components, Mater. Des. 135 (2017) 397–410.
[19] H.M. Wong, K.W. Yeung, K.O. Lam, V. Tam, P.K. Chu, K.D. Luk, K.M. Cheung, A biodegradable polymer-based coating to control the performance of magnesium alloy orthopaedic implants, Biomaterials 31 (2010) 2084–2096.
[20] J. Wang, Y. Ma, S. Guo, W. Jiang, Q. Liu, Effect of Sr on the microstructure and biodegradable behavior of Mg–Zn–Ca-Mn alloys for implant application, Mater. Des. 153 (2018) 308–316.
[21] B. Zhang, Y. Hou, X. Wang, Y. Wang, L. Geng, Mechanical properties, degradation performance and cytotoxicity of Mg-Zn-Ca biomedical alloys with different compositions, Mater. Sci. Eng. C 31 (2011) 1667–1673.
[22] F. Rosalbino, S. De Negri, G. Scavino, A. Saccone, Microstructure and in vitro degradation performance of Mg-Zn-Mn alloys for biomedical application, J. Biomed. Mater. Res. Part A 101 (2013) 704–711.
[23] M. Pogorielov, E. Husak, A. Solodivnik, S. Zhdanov, Magnesium based biodegradable alloys: degradation, application, and alloying elements, Interv. Med. Appl. Sci. 9 (2017) 27–38.
[24] M.H. Tsai, M.S. Chen, L.H. Lin, M.H. Lin, C.Z. Wu, K.L. Ou, C.H. Yu, Effect of heat treatment on the microstructures and damping properties of biomedical Mg–Zr alloy, J. Alloy. Compd. 509 (2011) 813–819.
[25] Y. Li, C. Wen, D. Mushahary, R. Sravanthi, N. Harishankar, G. Pande, P. Hodgson, Mg–Zr–Sr alloys as biodegradable implant materials, Acta Biomater. 8 (2012) 3177–3188.

[26] Y. Chen, J. Yan, Z. Wang, S. Yu, X. Wang, Z. Yuan, X. Zhang, C. Zhao, Q. Zheng, In vitro and in vivo corrosion measurements of Mg–6Zn alloys in the bile, Mater. Sci. Eng. C 42 (2014) 116–123.
[27] S.S. Wong, L.C. Chan, C.P. Lai, W.Y. Ip, L.H. Chau, In vitro and in vivo degradation evaluation of Mg-based alloys for biomedical applications, J. Mater. Sci. Technol. Res. 2 (2015) 7–16.
[28] C.E. Wen, Y. Yamada, K. Shimojima, Y. Chino, H. Hosokawa, M. Mabuchi, Compressibility of porous magnesium foam: dependency on porosity and pore size, Mater. Lett. 58 (2004) 357–360.
[29] G. Jia, Y. Hou, C. Chen, J. Niu, H. Zhang, H. Huang, M. Xiong, G. Yuan, Precise fabrication of open porous Mg scaffolds using NaCl templates: relationship between space holder particles, pore characteristics and mechanical behavior, Mater. Des. 140 (2018) 106–113.
[30] M. Cheng, T. Jiang, W. Fu, G. Jiang, W. Liu, Y. Qiao, X. Peng, T. Cheng, X. Zhang, G. He, X. Liu, A novel open-porous magnesium scaffold with controllable microstructures and properties for bone regeneration, Sci. Rep. 6 (2016), 24134.
[31] T. Adachi, Y. Osako, M. Tanaka, M. Hojo, S.J. Hollister, Framework for optimal design of porous scaffold microstructure by computational simulation of bone regeneration, Biomaterials 27 (2006) 3964–3972.
[32] L. Xiong, C.K. Chui, C.L. Teo, D.P.C. Lau, Modeling and simulation of material degradation in biodegradable wound closure devices, J. Biomed. Mater. Res. Part B 102 (2014) 1181–1189.
[33] K.B. Deshpande, Validated numerical modelling of galvanic corrosion for couples: magnesium alloy (AE44)–mild steel and AE44–aluminium alloy (AA6063) in brine solution, Corrosion Sci 52 (2010) 3514–3522.
[34] N. Debusschere, P. Segers, P. Dubruel, B. Verhegghe, M. De Beule, A finite element strategy to investigate the free expansion behaviour of a biodegradable polymeric stent, J. Biomech. 48 (2015) 2012–2018.
[35] K.B. Deshpande, Numerical modeling of micro-galvanic corrosion, Electrochim. Acta 56 (2011) 1737–1745.
[36] X.N. Gu, Y.F. Zheng, A review on magnesium alloys as biodegradable materials, Front Mater Sci China 4 (2010) 111–115.
[37] W. Wu, S.S. Chen, D. Gastaldi, L. Petrini, D. Mantovani, K. Yang, L.L. Tan, F. Migliavacca, Experimental data confirm numerical modeling of the degradation process of magnesium alloys stents, Acta Biomater. 9 (2013) 8730–8739.
[38] J.A. Grogan, B.J. O'Brien, S.B. Leen, P.E. McHugh, A corrosion model for bioabsorbable metallic stents, Acta Biomater. 7 (2011) 3523–3533.
[39] D. Gastaldi, V. Sassi, L. Petrini, M. Vedani, S. Trasatti, F. Migliavacca, Continuum damage model for bioresorbable magnesium alloy devices—application to coronary stents, J. Mech. Behav. Biomed. Mater. 4 (2011) 352–365.
[40] J.A. Grogan, S.B. Leen, P.E. McHugh, A physical corrosion model for bioabsorbable metal stents, Acta Biomater. 10 (2014) 2313–2322.
[41] E.L. Boland, R. Shine, N. Kelly, C.A. Sweeney, P.E. McHugh, A review of material degradation modelling for the analysis and design of bioabsorbable stents, Ann. Biomed. Eng. 44 (2016) 341–356.
[42] M.Q. Cheng, T. Wahafu, G.F. Jiang, W. Liu, Y.Q. Qiao, X.C. Peng, T. Cheng, X.L. Zhang, G. He, X.Y. Liu, A novel open-porous magnesium scaffold with controllable microstructures and properties for bone regeneration, Sci. Rep. 6 (2016), 24134.
[43] M. Yazdimamaghani, M. Razavi, D. Vashaee, K. Moharamzadeh, A.R. Boccaccini, L. Tayebi, Porous magnesium-based scaffolds for tissue engineering, Mater. Sci. Eng. C 71 (2017) 1253–1266.
[44] L.C. Chan, X.Z. Lu, C.P. Lai, L.W.P. Chow, Compressive behaviours of raw and cased porous magnesium-alloys determined by X-ray CT, Procedia Eng 207 (2017) 1427–1432.
[45] D. Lin, D. Luo, K. Lian, W. Zhai, Z. Ding, Reconstruction of traumatic bone defect with in situ implantation of dropped traumatic segmental bone fragments, Orthopedics 39 (2016) e14–e18.
[46] N. Sezer, Z. Evis, S.M. Kayhan, A. Tahmasebifar, M. Koç, Review of magnesium-based biomaterials and their applications, J. Magnes. Alloy. 6 (2018) 23–43.
[47] D. De Cicco, F. Taheri, Enhancement of magnesium-composite bond-interface by a simple combined abrasion and coating method, J. Magnes. Alloy. 7 (2019) 227–239.
[48] Y. Lin, S. Cai, S. Jiang, D. Xie, R. Ling, J. Sun, J. Wei, K. Shen, G. Xu, Enhanced corrosion resistance and bonding strength of Mg substituted β-tricalcium phosphate/Mg $(OH)_2$ composite coating on magnesium alloys via one-step hydrothermal method, J. Mech. Behav. Biomed. Mater. 90 (2019) 547–555.
[49] ASTM, Standard Guide for Laboratory Immersion Corrosion Testing of Metals, ASTM G31-12a, ASTM International, West Conshohocken, PA, 2012.
[50] N.T. Kirkland, J. Waterman, N. Birbilis, G. Dias, T.B.F. Woodfield, R.M. Hartshorn, M.P. Staiger, Buffer-regulated biocorrosion of pure magnesium, J. Mater. Sci. Mater. Med. 23 (2012) 283–291.
[51] ASTM, Standard Test Methods of Compression Testing of Metallic Materials at Room Temperature, ASTM E9-09, ASTM International, West Conshohocken, PA, 2009.
[52] X.Z. Lu, L.C. Chan, Micromechanics-based damage model for failure prediction in cold forming, Mater. Sci. Eng. A 690 (2017) 120–131.
[53] ASTM, Standard Practice for Short-Term Screening of Implant Materials, ASTM F763-04 (2016), ASTM International, West Conshohocken, PA, 2016.
[54] G. Rousselier, Dissipation in porous metal plasticity and ductile fracture, J. Mech. Phys. Solids 49 (2001) 1727–1746.
[55] S. Pal, Design of Artificial Human Joints & Organs, Springer US, Boston, MA, 2014.
[56] G.Y. Li, J.S. Lian, L.Y. Niu, Z.H. Jiang, Q. Jiang, Growth of zinc phosphate coatings on AZ91D magnesium alloy, Surf. Coat. Technol. 201 (2006) 1814–1820.
[57] L. Kouisni, M. Azzi, M. Zertoubi, F. Dalard, S. Maximovitch, Phosphate coatings on magnesium alloy AM60 part 1: study of the formation and the growth of zinc phosphate films, Surf. Coat. Technol. 185 (2004) 58–67.
[58] B. Zberg, P.J. Uggowitzer, J.F. Löffler, MgZnCa glasses without clinically observable hydrogen evolution for biodegradable implants, Nat. Mater. 8 (2009) 887–891.
[59] Y.J. Liu, Z.Y. Yang, L.L. Tan, H. Li, Y.Z. Zhang, An animal experimental study of porous magnesium scaffold degradation and osteogenesis, Brazilian J. Med. Biol. Res. 47 (2014) 715–720.
[60] A. Chaya, S. Yoshizawa, K. Verdelis, N. Myers, B.J. Costello, D.-T. Chou, S. Pal, S. Maiti, P.N. Kumta, C. Sfeir, In vivo study of magnesium plate and screw degradation and bone fracture healing, Acta Biomater. 18 (2015) 262–269.
[61] J. Kuhlmann, I. Bartsch, E. Willbold, S. Schuchardt, O. Holz, N. Hort, D. Höche, W.R. Heineman, F. Witte, Fast escape of hydrogen from gas cavities around corroding magnesium implants, Acta Biomater. 9 (2013) 8714–8721.
[62] H. Zhuang, Y. Han, A. Feng, Preparation, mechanical properties and in vitro biodegradation of porous magnesium scaffolds, Mater. Sci. Eng. C 28 (2008) 1462–1466.